\$ SUPER

Contents lists available at ScienceDirect

Optical Materials

journal homepage: www.elsevier.com/locate/optmat





The role of glass composition in the 3D laser fabrication of lithium niobate single crystal in lithium niobosilicate glass

Keith Veenhuizen ^{a,*}, Collin Barker ^b, Jacob Franklin ^a, Sean McAnany ^c, Bruce Aitken ^d, Daniel Nolan ^d, Volkmar Dierolf ^b, Himanshu Jain ^c

- a Department of Physics, Lebanon Valley College, USA
- ^b Department of Physics, Lehigh University, USA
- ^c Department of Materials Science and Engineering, Lehigh University, USA
- ^d Corning Incorporated, USA

ARTICLE INFO

Keywords: Lithium niobate Silicate glass Femtosecond laser Laser-induced crystallization Single crystal

ABSTRACT

Spatially selective growth of lithium niobate (LiNbO $_3$) crystals deep within lithium niobosilicate (LNS) glass can be achieved via femtosecond laser irradiation, wherein these crystals could serve as optical elements in photonic integrated circuits. In practice, it is challenging to achieve continuous, single-crystal growth of LiNbO $_3$ within LNS glass. This work reports on progress in overcoming this challenge by exploring how the formation of single-crystal LiNbO $_3$ is influenced by the incongruent composition of the glass matrix. An investigation of the parameter space of glass composition ((100-x) LiNbO $_3-x$ SiO $_2$ for x=22, 26, 30, and 34), laser scanning speed, and laser power leads to the observation of several growth modes: continuous growth at an optimal speed, segmented growth below it, and polycrystalline growth above it. For certain glass compositions, a balance of long incubation time and high crystal growth rate results in the ability to grow indefinitely long (\sim cm) single crystal lines at the optimal scanning speed. Guidance for predicting which glass compositions are most suitable for single crystal growth based on the LNS composition diagram is provided.

1. Introduction

Laser irradiation of dielectric media has been studied extensively for its ability to create a variety of modifications with spatial selectivity. These modifications include refractive index changes in glass [1], laser-inscribed damage tracks [2], crystals in glass [3], etc., all of which have the potential to be used as optical elements in photonic integrated circuits. Depending on the type of laser utilized, these modifications can be localized near the surface (when using continuous wave lasers) or made deep within the material (by employing pulsed lasers). This difference in location owes to the absorption mechanism, which is linear absorption for the former and nonlinear absorption for the latter. Besides three-dimensional spatial selectivity in forming a modification, the nonlinear absorption mechanism observed with pulsed lasers has the potential for a richer range of laser-matter interactions, such as nanogratings [4], color centers [5], etc.

Laser-induced crystallization of glass, in particular, has attracted attention since crystals can serve not only as passive waveguides but also as active elements. Laser-induced crystallization of glass has been

demonstrated in a variety of systems including chalcogenides such as Sb-S-I [6,7] and oxides such as LaBGeO₅ [8-10] and lithium niobosilicate (LNS) [11,12]. Crystallization of LNS glass shows promise for practical application since it crystallizes into LiNbO3, a material possessing favorable nonlinear optical coefficients [13] and electro-optic coefficients [14]. Anisotropic crystals can be formed via laser irradiation, as is the case in LNS, for which a detailed understanding of the morphology (polycrystal, segmented crystal, or continuous crystal) and orientation of the resulting crystal is essential for potential device applications. For example, for passive waveguiding purposes alone, the anisotropic crystal should be a continuous, single crystal line to eliminate optical losses due to grain boundaries. For active applications such as an electro-optic modulator, the electro-optic coefficients that can be utilized depends on the crystal orientation and the phase-shift that can be applied to the guided light depends on the length to which the crystal can be grown.

Multiple groups have reported on various morphologies of $LiNbO_3$ which can be precipitated with the femtosecond (fs) laser, such as nanocrystal [12] and segmented crystal [11]. Mechanisms for

E-mail address: veenhuiz@lvc.edu (K. Veenhuizen).

 $^{^{\}ast}$ Corresponding author.

understanding and controlling fs laser crystallization have been proposed in a four-component lithium niobium borosilicate glass [15]. However, the formation of continuous ${\rm LiNbO_3}$ single crystal architecture in glass with fs laser, as would be desirable for certain optical applications, has not yet been achieved. Additionally, the effect of the fraction of glass former, i.e. ${\rm SiO_2}$, on crystal formation in the three-component lithium niobosilicate glass has not been reported in the literature. Through a systematic variation of parameters such as glass composition, laser scanning speed, and laser power, new insight can be gained on the reasons for the formation of continuous, single crystal as well as other morphologies.

This work reports on the influence of LNS glass composition on the laser-induced crystallization of LiNbO3. The glasses utilized have the Li2O to Nb2O5 ratio fixed at 1 while the fraction of SiO2 is varied. It will be shown that the incubation time and maximum crystal growth rate depend on glass composition. Formation of crystals of various morphologies can be obtained via systematic control of the processing parameters. Mechanisms for the observed crystallization tendencies are discussed. Most notably, we will demonstrate that LiNbO3 single crystals of effectively unlimited length can be grown in LNS glasses of certain compositions due to their favorable nucleation and crystal growth behaviors.

2. Methods

Four compositions of lithium niobosilicate glass were made using the conventional melt-quenching technique. These compositions are (100 – x) LiNbO $_3$ – x SiO $_2$, where x = 22, 26, 30, and 34 (mol%). These glasses are hereafter referred to as LNSx. High-purity reagents of Li $_2$ CO $_3$ (99.999%), Nb $_2$ O $_5$ (99.9985%), and SiO $_2$ (99.99%) were mixed into 40 g batches and melted in a Pt–Rh crucible at 1400 °C for 1 h. The melt was quenched by pouring it onto a steel plate at room temperature and pressing another steel plate on top. The glass samples were subsequently annealed in a furnace at 500 °C for 2 h, after which the furnace was cooled to room temperature. The composition of each glass was determined using inductively coupled plasma optical emission spectroscopy (for Nb and Si) and flame emission spectroscopy (for Li).

The glass transition (T_g), onset crystallization (T_x), and peak crystallization (T_p) temperatures of each glass composition were measured using differential scanning calorimetry (DSC) (model: 404 Pegasus F3, Netzsch, Selb, Germany). The samples were heated from room temperature to 950 °C at a rate of 10 C°/min. Through repeated trials, the uncertainty in the measurement of T_g was found to be 0.5 °C, and the uncertainty in the measurements of T_x and T_p were found to be 3 °C.

Glass samples were polished optically smooth for laser-induced crystallization experiments. Prior to laser-irradiation, it was verified through Raman spectroscopy and X-ray diffraction that the samples were amorphous (for Raman spectra of these glasses, see Refs. [11,16]). Previous studies of this glass system have established LNS crystallizes into LiNbO3 [11,17]. To fabricate LiNbO3 crystals in glass, a PHAROS femtosecond laser (model: SP-06-200-PP, Light Conversion, Vilnius, Lithuania) with a wavelength of 1026 nm, repetition rate of 200 kHz and pulse duration of 175 fs was focused at an actual depth of 200 μ m below the surface of the glass samples using a 50X, 0.6 NA Nikon extra-long working distance objective lens. The sample was mounted on a stage that was heated to 500 °C to avoid cracking during laser irradiation.

Two sets of measurements were performed. In one type of experiment, the laser was focused to a fixed position within the glass while measuring the time it takes for a LiNbO₃ crystal to form. LiNbO₃ crystal possesses second-order optical nonlinearity. When the crystal is present, it causes second harmonic generation where the incident 1026 nm laser is scattered at half the wavelength, resulting in the emission of green light [17]. The glass itself does not cause second harmonic generation, so green light emission confirms the formation of LiNbO₃ crystal. By measuring the time from the start of laser irradiation to when green light first appears, the incubation time (i.e. the time for forming observable

crystal) in each glass composition could be compared. For each composition, 50 trials were conducted. The laser power was kept the same for all trials (550 mW, or 2.75 μJ per pulse). The second set of experiments consisted of fabricating crystal lines by translating the laser focus at a fixed depth within the glass using a motorized stage upon which the sample was mounted. Throughout the time of translating the laser, second harmonic generation was observed, indicating the growth of LiNbO $_3$ crystal. Crystal lines were made by systematically varying the translation speed from 5 to 55 $\mu m/s$ and laser power from 415 to 830 mW (2.08–4.15 μJ per pulse). The laser power was measured after the objective. For all crystal lines, the laser polarization was fixed parallel to the laser scanning direction.

Crystals produced by the second experiment were characterized by electron backscatter diffraction (EBSD) using a Hitachi 4300SE scanning electron microscope. The crystal lines embedded within the glass were brought to the surface by polishing it with diamond lapping film sheets to a 0.1 μm finish. EBSD measurements allowed for a spatially resolved determination of the orientation of the crystal lattice. Crystals could be distinguished as either single crystal or polycrystalline, and crystal growth at the same processing parameters (laser scanning speed and laser power) could be systematically compared between glass compositions.

3. Results

Table 1 shows the nominal and actual composition of glasses used in this study. The nominal Li/Nb ratio was fixed at 1 while varying the amount of ${\rm SiO_2}$. For LNS26 and LNS34, the actual and nominal compositions exactly match. For LNS22 and LNS30, there is a slight excess of Nb₂O₅.

DSC scans for each glass composition are shown in Fig. 1 (measured values for T_g , T_x , and T_p are reported in Table 1). With increasing amounts of SiO₂, the glass transition temperature increases from 550 to 567 °C, consistent with the results of Prapitpongwanich et al. [18]. From LNS22 to LNS30, the onset crystallization temperature increases by 52 C°, before dropping slightly by 2 C° from LNS30 to LNS34.

Box plots of the incubation time measurements in each glass composition are shown in Fig. 2. The incubation time strongly depends on the glass composition. The shortest times occur for LNS22, with no time exceeding 15 s. For LNS30, no time falls below 15 s. The median times for LNS 22, 26, 30, and 34 are 1.6 s, 28 s, 230 s, and 30 s, respectively. The times differ across two orders of magnitude, with the median time increasing from LNS22 to LNS30 before decreasing from LNS30 to LNS34.

The fs laser was also used to make crystal lines with systematically varied laser processing parameters for each glass composition. For all crystal lines, the laser was fixed in position until a crystal formed; thereafter, the laser was scanned at a constant speed. Figures in this article will primarily focus on crystal growth in LNS22, LNS26, and LNS34 since crystallization in LNS30 was reported extensively by the current authors in a past publication [11]. In the Discussion section, however, crystallization in all four compositions will be analyzed, with reference made to Ref. [11] as needed.

Fig. 3a shows an optical image of crystal lines fabricated with the same laser power (630 mW) at various laser scanning speeds in LNS26. For lower scanning speeds (less than 45 $\mu m/s$), the crystal growth is repeatedly interrupted, resulting in the segmented appearance of the crystal line. With increasing scanning speed (from 15 to 35 $\mu m/s$), the average segment length increases. At an optimal scanning speed, 45 $\mu m/s$ for LNS26, growth of a continuous crystal is achieved. At 55 $\mu m/s$, discontinuous growth occurs where the crystal width periodically tapers.

The optical image only shows the morphology of the laser modifications without detailing the crystallinity. Fig. 3b shows longitudinal (i. e. a view of the crystal in the xy plane along its length, see the diagram in the figure) X-axis inverse pole figure (IPF) maps collected via EBSD for

Table 1

Nominal compositions and actual compositions measured by chemical analysis. Glass transition temperature, onset crystallization temperature, and peak crystallization temperature measured from DSC for each glass sample.

	Nominal composition (mol %)			Actual composition (mol %)			DSC Results		
sample	SiO ₂	Li ₂ O	Nb ₂ O ₅	SiO ₂	Li ₂ O	Nb ₂ O ₅	T _g (°C)	T _x (°C)	T _p (°C)
LNS22	22	39	39	21	39	40	550	655	662
LNS26	26	37	37	26	37	37	558	672	687
LNS30	30	35	35	30	34	36	563	707	721
LNS34	34	33	33	34	33	33	567	705	715

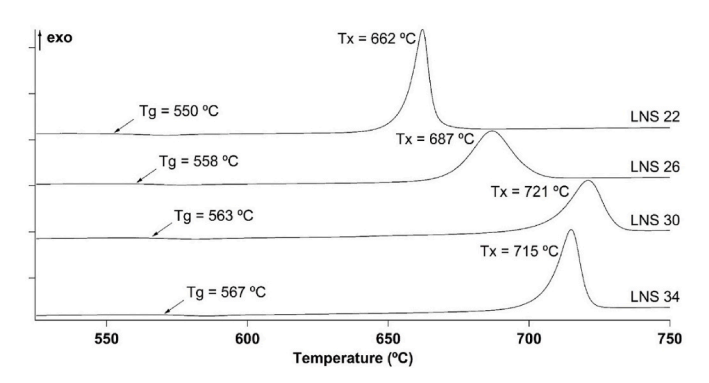


Fig. 1. DSC curves for LNS22, LNS26, LNS30, and LNS34 obtained using a heating rate of 10 $\rm C^0/min.$

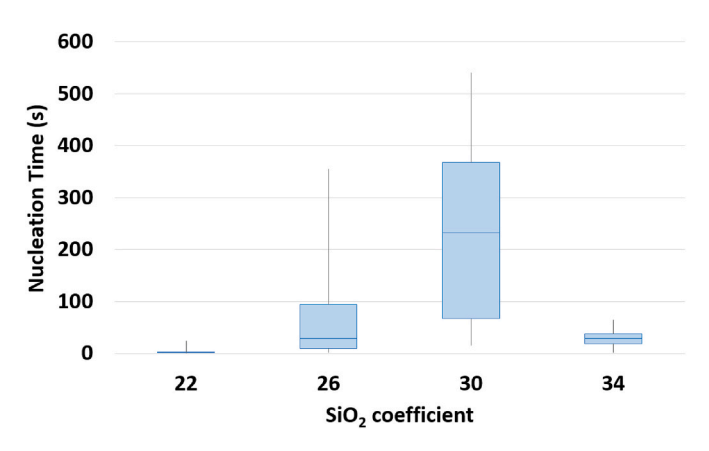


Fig. 2. Box plots of incubation time as a function of glass composition. Each box plot shows the minimum, first quartile, median, third quartile, and maximum for that data set. For each glass composition, 50 trials were conducted. The laser power was set to 550 mW for all trials.

crystal lines written at 45 and 50 μ m/s. An image quality overlay is used to differentiate amorphous regions, where a Kikuchi pattern was absent, from crystalline regions. The overlay makes glassy areas appear dark. The colors indicate the crystal direction aligned with the X-axis (i.e. aligned with the laser scanning direction).

The consistent coloration for the line written at 45 $\mu m/s$ demonstrates it is not only continuous but single crystal. At this scanning speed, continuous, single crystal growth can be maintained indefinitely (in the experimental setup available, for several cm) and was verified by performing EBSD along its length. The red color in the IPF map indicates the crystal has its c-axis oriented parallel to the laser scanning direction, as observed in previous studies of this glass system [11]. Above this optimal scanning speed, the growth is polycrystalline, as indicated by the grain boundary in the line written at 50 $\mu m/s$ in Fig. 3b.

Fig. 4 shows longitudinal EBSD scans of crystals made in LNS34 glass at a variety of scan speeds and fixed power (415 mW). Similar to LNS26, there is a transition from segmented growth at low speeds to

polycrystalline growth at high speeds. In contrast to LNS26, all lines were observed to be polycrystalline for LNS34. With increasing scan speed, the size of individual grains reduces to a few microns and the fractional volume which is crystallized as compared to glass also decreases.

The difference in crystal growth in glasses of different composition is even more apparent in Fig. 5. Fig. 5a and b shows crystals fabricated in LNS34 and LNS22 where the same laser processing parameters were used in both glasses. In LNS34, the lines are highly polycrystalline. In LNS22, however, the lines possess a much greater crystallized volume and fewer grains. Fig. 5c shows that at 25 $\mu m/s$, crystals grown in LNS34 exhibit the polycrystalline growth mode, while even at 45 $\mu m/s$, the crystallized volume in LNS22 is greater with crystal grains possessing a size upwards of 20 μm . As was observed for LNS34, all lines were observed to be polycrystalline in LNS22.

4. Discussion

The difference in crystallization behavior of each glass can be explained by the variation of nucleation and growth with glass composition and the effect of laser scanning speed on crystal growth. Focusing first on crystallization in LNS22 and LNS34, the results of Fig. 5 show the crystal growth rate in LNS22 exceeds that of LNS34. At a laser scanning rate of $35 \,\mu\text{m/s}$ (Fig. 5a), individual crystals can freely nucleate in LNS34, but their growth rate is not high enough to keep pace with the laser, causing the observed polycrystalline growth mode. In contrast, at the same laser scanning speed, the higher crystal growth rate in LNS22 results in a larger crystallized volume and allows for grains to grow with the laser for longer distances. In other silicate systems, increasing the amount of SiO₂ relative to the glass modifier (Li) increases the viscosity [19]. As such, LNS34 is expected to have a greater viscosity compared to LNS22. The increase in viscosity lowers the chemical diffusion and hence would lower the crystal growth rate in LNS34 compared to LNS22.

Following the work of Poumellec et al. [15], these observations can be better understood using a time-temperature-transformation (TTT) diagram. The TTT diagram in Fig. 6 shows schematically the crystallization domains for LNS34 and LNS22 in blue and red, respectively. The crystallization domain for LNS22 extends to shorter times since its incubation time shown in Fig. 2 is lower compared to LNS34. The low temperature bound of the crystallization domain is dictated by $T_{\rm g}$. Based on the DSC results in Fig. 1, the crystallization domain for LNS22 should extend to lower temperatures compared to LNS34. The temperature as a function of time for a given position in the glass as the laser focus passes through it is represented by the purple and orange curves, where the orange curve corresponds to a slower laser scanning speed.

The orange curve spends less time in the crystallization domain for LNS34 as compared to LNS22. This results in a smaller fractional volume that crystallizes in LNS34 compared to LNS22, in agreement with all cases where identical laser processing parameters were used in these two glasses (see Fig. 5a and b).

The effect of laser scanning speed on crystal growth shown in Fig. 4 can also be explained with the TTT diagram. The purple curve in Fig. 6 corresponds to a faster laser scanning speed. This curve intersects the crystallization domain for LNS34 for less time as compared to the orange curve. Accordingly, it results in a smaller fractional volume that

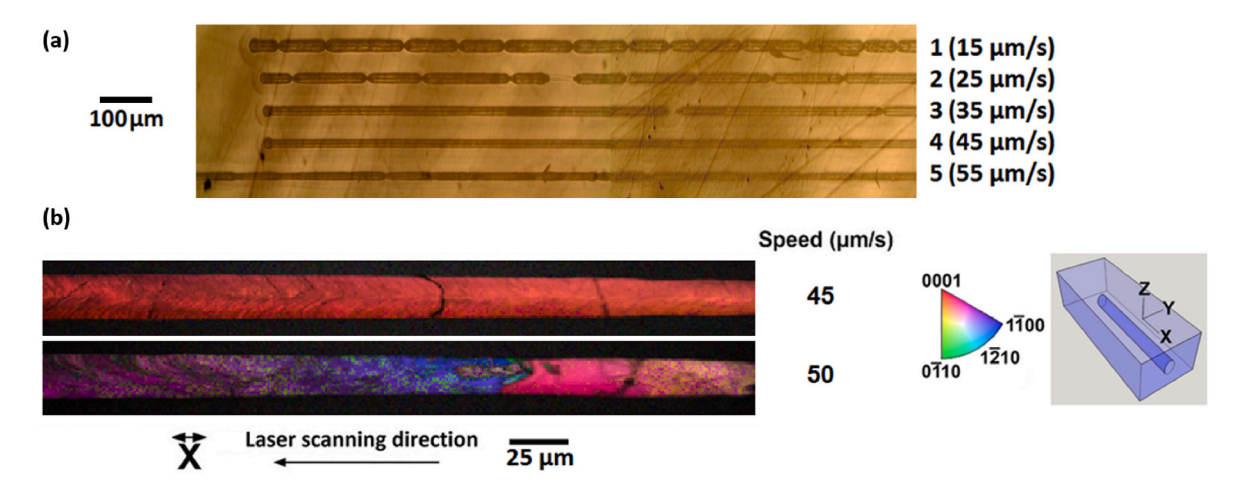


Fig. 3. (a) Optical image of crystal lines grown in LNS26 glass at various laser scanning speeds. Scale bar for optical image corresponds to $100 \mu m$. (b) Longitudinal X-axis IPF maps of crystal lines grown with laser scanning speeds of 45 and 50 $\mu m/s$. Laser power set to 630 mW for all crystal lines shown in this figure. Scale bar for IPF map corresponds to $25 \mu m$.

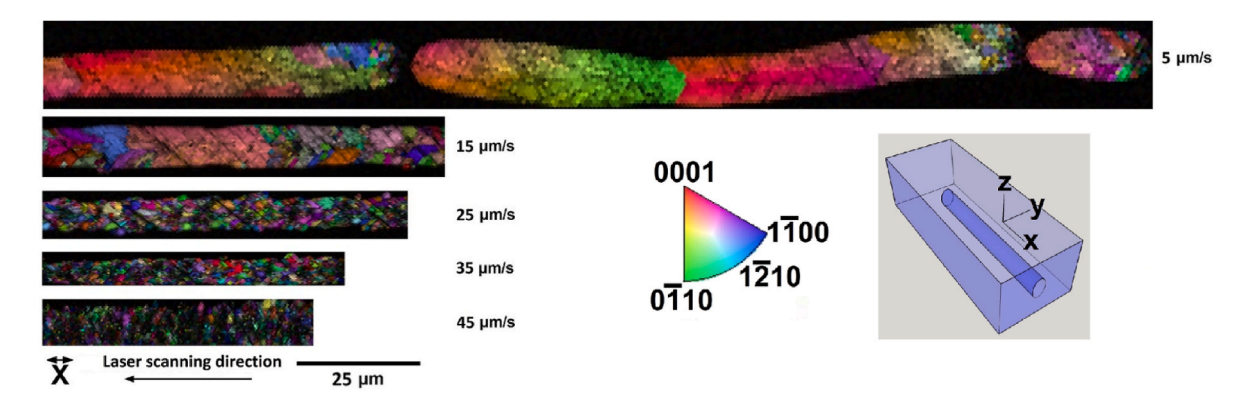


Fig. 4. Longitudinal X-axis IPF maps of crystal lines grown in LNS34 glass at a fixed laser power (415 mW) and various laser scanning speeds. Scale bar corresponds to $25 \mu m$.

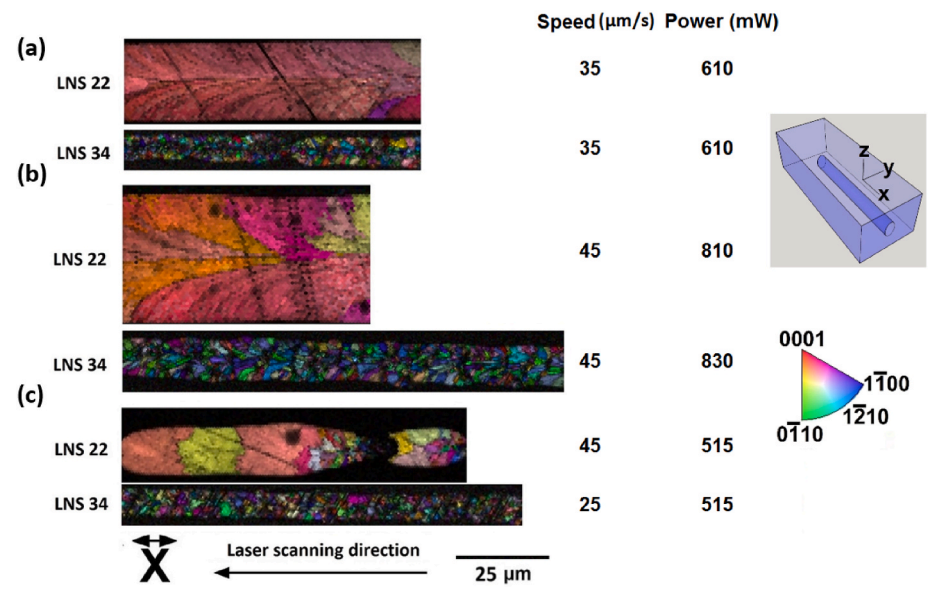


Fig. 5. Longitudinal X-axis IPF maps of crystal lines grown in LNS22 and LNS34 glasses for the laser processing parameters listed. Scale bar correspond to 25 µm.

K. Veenhuizen et al. Optical Materials 128 (2022) 112380

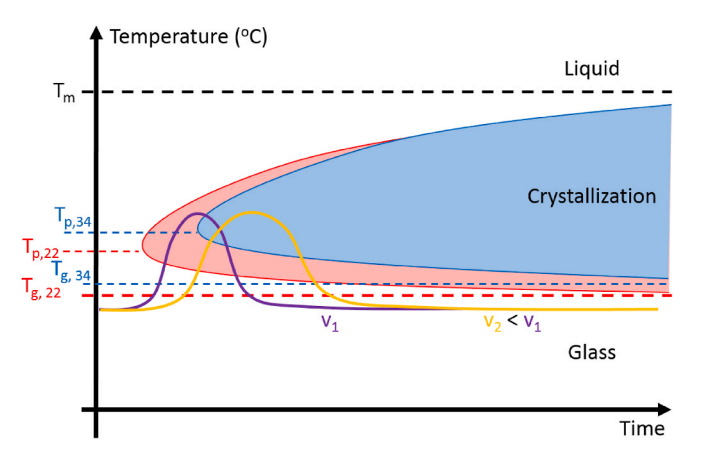


Fig. 6. Time-temperature-transformation diagram modeling the variation in laser-induced crystal growth with glass composition. The crystallization domain for LNS34 and LNS22 are shown in blue and red, respectively. The crystallization domain extends to shorter times for LNS22 due to its shorter incubation time (see Fig. 2). It also extends to lower temperatures since the T_p and T_g for LNS22 are lower (See Fig. 1). The purple and orange curves show the temperature as a function of time at a fixed position in the glass as the laser scans through it at speed v, where $v_2 < v_1$. (For interpretation of the references to color in this figure legend, the reader is referred to the Web version of this article.)

crystallizes when the laser scanning speed is faster, consistent with the results in Fig. 4.

The results of Fig. 3 further demonstrate the interplay between laser scanning speed and crystal growth rate. Below the optimal scanning speed, segmented growth occurs. Segmented growth has been observed previously during continuous wave laser irradiation of NiO-doped LNS glasses [20] and fs laser irradiation of LaBGeO₅ [21] and LNS glasses [11]. Such a morphology is the result of nucleation, crystal growth, and interruption of growth, after which nucleation starts the process again. The interruption in growth is caused by a temporary disruption in heat accumulation near the laser focus [21]. The disruption is a result of the crystal scattering the laser before it reaches the focus. This happens because a steady state crystal growth front cannot be achieved when the crystal growth rate exceeds the laser scanning speed [21]. After the interruption, while the laser translates back into the glass, it has a negligible effect on the previously formed crystal due to the lack of heating. That crystal line is stable unless another pass is made by the laser [22]. Upon the laser translating into the glass, absorption and heat accumulation are re-initiated, leading to nucleation and growth of a new segment. As the laser scanning speed is increased, it eventually matches the maximum crystal growth rate, allowing for a stable crystal growth front and continuous crystal growth. This occurs at 45 μ m/s in LNS26.

A crucial question then arises as to why it is possible to achieve continuous, single crystal lines in LNS26 but not in LNS22 and LNS34. It comes down to a balance of nucleation and growth, as mediated by the laser scanning rate. LNS26 and LNS34 possess similar incubation times, as evidenced by Fig. 2. The crystal growth rate, however, is higher in LNS26 as compared to LNS34. Because of this, after the initial formation of a crystal seed in LNS26, extra nucleation can be suppressed by scanning at high speeds, as discussed previously by Savytskii et al. in their work on growing Sb₂S₃ single crystal in Sb-S-I glass [23]. Since LNS34 has a lower crystal growth rate, the laser scanning speed must be lowered to ensure continuous crystal growth, but at this low speed, unwanted nucleation occurs, preventing single crystal growth. Comparing LNS22 and LNS26, the results show that the crystal growth rate is relatively high for both. The incubation time, however, is shorter in LNS22 than in LNS26 by an order of magnitude, according to Fig. 2. As such, the strategy of eliminating extra nucleation by scanning at high speeds does not work in LNS22, resulting in the polycrystalline lines

observed in Fig. 5.

The results of Ref. [11] can be further understood in the context of the current work. Due to the greater amount of SiO_2 in LNS30, it possesses a lower crystal growth rate compared to LNS26. If LNS30 had a comparable incubation time to LNS26, single crystal formation could not be achieved in LNS30 because the laser scanning rate required to eliminate extra nucleation would exceed the crystal growth rate in this composition. This would lead to the same situation as for LNS34. But the results of Fig. 2 show that LNS30 has a greater incubation time by an order of magnitude as compared to LNS26. The greater incubation time affords the opportunity to scan the laser at a lower rate, allowing for the formation of single crystal at 25 $\mu m/s$ in LNS30 [11].

To summarize, LNS34 is characterized by a slow crystal growth rate and long nucleation time while LNS22 possesses a fast crystal growth rate and short nucleation time. As discussed above, neither of these situations is favorable for single crystal formation. By contrast, the balance of long nucleation time and fast crystal growth rate in LNS26 makes it ideal for growing single crystals. LNS30 possesses a longer incubation time compared to LNS26. As such, the laser scanning rate does not have to be set to as high a speed in LNS30 as compared to LNS26 to suppress nucleation and ensure single crystal growth.

An interesting possibility is predicting beforehand which among these compositions is most conducive to single crystal growth by referring to the LNS ternary composition diagram. Fig. 7 (modified from Ref. [24]) shows the glass forming region according to two different research groups, group 1 [25] and group 2 [26]. Both groups report that LNS34 lies within the glass forming region. LNS26 and LNS30 lie just outside the glass forming region according to group 1 while group 2 reports that LNS26 and LNS30 can form a glass. LNS22 lies well outside the glass forming region according to group 1. Group 2 reports that LNS22 can form a glass, but it is near their observed boundary of the glass forming region. Moving too far outside the glass forming region leads to uncontrolled nucleation, as in LNS22. Moving too far within the glass forming region with the addition of SiO2, as with LNS34, reduces the crystal growth rate significantly. Among the compositions studied, it is thus reasonable to suggest that LNS26 and LNS30 are most promising for single crystal growth because they lie at the boundary of the glass forming region.

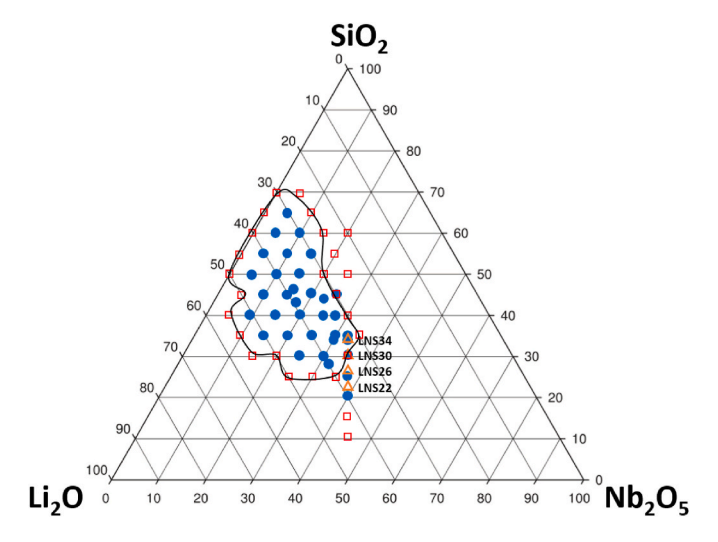


Fig. 7. LNS composition diagram reproduced from Ref. [24]. It shows glass formation according to groups 1 [25] and 2 [26] as filled blue circles and crystallization according to groups 1 and 2 as open red squares. Modified from Ref. [24] to show the boundary of the glass forming region according to group 1 (shown as a solid black line) and to include the glass compositions used in this work (shown as open orange triangles). © 2016 The American Ceramic Society. (For interpretation of the references to color in this figure legend, the reader is referred to the Web version of this article.)

5. Conclusions

Lithium niobate crystals were fabricated in four compositions of lithium niobosilicate glass to understand how fs laser-induced crystal-lization is influenced by the glass former (SiO_2) mole fraction. It was observed that the incubation time is shortest in LNS22. Incubation times in LNS26 and LNS34 are comparable to one another and longer than in LNS22. The crystal growth rate was observed to be the lowest in LNS34 as compared to LNS22 and LNS26.

The mechanism for why single crystal growth is possible in LNS26 but not LNS22 and LNS34 is proposed to be an interplay of nucleation and growth. Specifically, LNS26 has a suitably long incubation time and high crystal growth rate, allowing a single crystal to be grown at high speeds to make sure no other nuclei form. This cannot be achieved in LNS22 due to too short an incubation time nor in LNS34 due to too low a crystal growth rate. LNS30 possesses the longest incubation time of all compositions, allowing single crystal growth to occur at lower laser scanning speeds compared to LNS26.

This work also demonstrated that in LNS26, at an optimal laser scanning speed which matches the maximum crystal growth rate in this glass composition, continuous, single crystal ${\rm LiNbO_3}$ can be grown to effectively indefinite length. This observation opens up the possibility of utilizing these crystals in photonic integrated circuits as waveguides or active components.

CRediT authorship contribution statement

Keith Veenhuizen: Conceptualization, Investigation, Formal analysis, Visualization, Data curation, Writing – original draft. Collin Barker: Investigation, Formal analysis, Visualization. Jacob Franklin: Investigation. Sean McAnany: Conceptualization, Methodology. Bruce Aitken: Conceptualization, Methodology. Daniel Nolan: Conceptualization, Project administration. Volkmar Dierolf: Conceptualization, Project administration, Writing – review & editing. Himanshu Jain: Conceptualization, Project administration, Writing – review & editing.

Declaration of competing interest

The authors declare that they have no known competing financial interests or personal relationships that could have appeared to influence the work reported in this paper.

Acknowledgements

Financial support for this research is provided by the National Science Foundation via the GOALI program for collaboration between Lehigh University and Corning Incorporated (DMR-1508177).

References

- K. Miura, et al., Photowritten optical waveguides in various glasses with ultrashort pulse laser, Appl. Phys. Lett. 71 (1997) 3329.
- [2] D. Choudhury, J.R. Macdonald, A.K. Kar, Ultrafast laser inscription: perspectives on future integrated applications, Laser Photon. Rev. 8 (2014) 827.
- [3] T. Komatsu, Design and control of crystallization in oxide glasses, J. Non-Cryst. Solids 428 (2015) 156.
- [4] B. Zhang, et al., Single femtosecond laser beam induced nanogratings in transparent media mechanisms and applications, J. Materiomics 5 (2019) 1.
- [5] S. Gao, et al., Laser-induced color centers in crystals, Opt Laser. Technol. 146 (2022), 107527.
- [6] D. Savytskii, et al., Rotating lattice single crystal architecture on the surface of glass, Sci. Rep. 6 (2016) 36449.
- [7] C. Au-Yeung, et al., Effect of laser beam profile on rotating lattice single crystal growth in Sb₂S₃ model glass, Crystals 11 (2021) 36.
- [8] A. Stone, et al., Direct laser-writing of ferroelectric single-crystal waveguide architecture in glass for 3D integrated optics, Sci. Rep. 5 (2015) 10391.
- [9] S. McAnany, et al., Challenges of laser-induced single-crystal growth in glass: incongruent matrix composition and laser scanning rate, Cryst. Growth Des. 19 (2019) 4489.
- [10] A. Lipatiev, et al., Space-selective crystallization of glass by an optical vortex beam, CrystEngComm 22 (2020) 430.
- [11] K. Veenhuizen, et al., Fabrication of graded index single crystal in glass, Sci. Rep. 7 (2017) 44327
- [12] J. Cao, et al., Modifications in lithium niobium silicate glass by femtosecond laser direct writing: morphology, crystallization, and nanostructure, J. Opt. Soc. Am. B 34 (2016) 160.
- [13] R. Boyd, Nonlinear Optics, Elsevier, 2007.
- [14] R.S. Weis, T.K. Gaylord, Lithium niobate: summary of physical properties and crystal structure, Appl. Phys. A 37 (1985) 191.
- [15] E. Muzi, et al., Towards a rationalization of ultrafast laser-induced crystallization in lithium niobium borosilicate glasses: the key role of the scanning speed, Crystals 11 (2021) 290.
- [16] W. Sun, et al., Determination of the structure of lithium niobosilicate glasses by molecular dynamics simulation with a new Nb-O potential, Comput. Mater. Sci. 207 (2022), 111307.
- [17] C. Fan, et al., Three-dimensional photoprecipitation of oriented LiNbO₃-like crystals in silica-based glass with femtosecond laser irradiation, Opt. Lett. 37 (2012) 2955.
- [18] P. Prapitpongwanich, K. Pengpat, C. Rüssel, Phase separation and crystallization in LiNBO₃/SiO₂ glasses, Mater. Chem. Phys. 113 (2009) 913.
- [19] N. Bansal, R.H. Doremus, Handbook of Glass Properties, Elsevier, 1986.
- [20] M. Shimada, T. Honma, T. Komatsu, Laser patterning of oriented LiNbO₃ crystal particle arrays in NiO-doped lithium niobium silicate glasses, Int. J. Appl. Glass Sci. 9 (2018) 518.
- [21] A. Stone, et al., Femtosecond laser-writing of 3D crystal architecture in glass: growth dynamics and morphological control, Mater. Des. 146 (2018) 228.
- [22] S.V. Lotarev, et al., Ultrafast-laser vitrification of laser-written crystalline tracks in oxide glasses, J. Non-Cryst. Solids 516 (2019) 1.
- [23] D. Savytskii, et al., Demonstration of single crystal growth via solid-solid transformation of a glass, Sci. Rep. 6 (2016) 23324.
- [24] J. Cao, et al., Nanoscale phase separation in lithium niobium silicate glass by femtosecond laser irradiation, J. Am. Ceram. Soc. 100 (2017) 115.
- [25] O. Maksimova, et al., Properties and structure of glasses of the system Li₂O-Nb₂O₅-SiO₂, Izv. Akad. Nauk. Latv. SSR Ser. Khim. 5 (1975) 530.
- [26] C. Fan, Contribution to Nano or Micro Crystallization Induction in Silica-Based Glass by Femtosecond Laser Irradiation, Doctoral dissertation, Sud University, Paris, 2013. HAL.